AN EFFICIENT DRAG REDUCTION OF BLUFF BODIES BY TESSELLATION

N. Beratlis, K. Squires
School for Engineering of Matter, Transport and Energy
Arizona State University
Tempe, AZ
nberatlis@asu.edu
squires@asu.edu

E. Balaras
Department of Mechanical and Aerospace Engineering
The George Washington University
Washington, DC
balaras@gwu.edu

ABSTRACT

In this work a new method of passive drag reduction on bluff bodies by tessellation is presented. Wind-tunnel measurements on tessellated spheres reveal that the variation of the drag coefficient is similar to dimpled spheres, manifested by a sudden decrease in the drag coefficient at a critical Reynolds number followed by a nearly constant drag value in the post-critical regime. However, tessellated spheres can achieve a further 10%-15% drag reduction compared to dimples without shifting the critical Reynolds number. To further investigate the underlying physics leading to this reduction we also conducted Direct Numerical Simulations of both tessellated and dimpled spheres at $Re = 1.50 \times 10^5$. The predicted values of drag coefficient agree very well with the experiments and confirm the drag reduction. Analysis of the flow reveals that the tessellated panels introduce a smaller pressure "penalty" compared to dimples at the front part of the body. In addition, transition to turbulence occurs later and near the top of the body. As a result the boundary layer grows thinner and global separation is delayed by approximately 10°.

INTRODUCTION

Passive roughness elements such as trip wires, dimples, protrusions of different shapes, etc. are effective in reducing the drag force on bluff (i.e. sphere, cylinder) as well as streamlined (i.e. airfoils) bodies. Among the different types of elements dimples are very efficient in maintaining the low drag configuration for a large range of Reynolds numbers. An example is shown in Fig. 1, where the variation of the drag coefficient, $C_D = 2F_D/\rho U_\infty^2 A$, as a function of Reynolds number, $Re = U_\infty D/\nu$, (F_D is the drag force, U_∞ is the freestream velocity, D the diameter, A the projected area, and ρ, ν the density and kinematic viscosity of the fluid respectively) is plotted for smooth and dimpled spheres. For the former case the drag coefficient remains constant ($C_D \sim 0.5$) until the Reynolds number approaches a critical value (Re $\sim 3 \times 10^5$). At this point, which is usually referred to as *drag crisis*, C_D decreases

rapidly and hits a minimum, which is an order of magnitude lower ($C_D \sim 0.08$). With further increase in the Reynolds number the flow enters into the post-critical regime characterized by turbulent boundary layers on the surface of the sphere. In this regime the drag coefficient rises slowly with increasing Reynolds number.

In dimpled spheres the drag crisis happens at a much lower critical Reynolds number ($Re < 7 \times 10^4$ in Fig. 1). The critical value of the Reynolds number, as well as the attained minimum drag coefficient in the post-critical regime depend on the dimple geometry and arrangement. In general as the total dimple volume is increased the drag crisis is accelerated and the drag coefficient in the post-critical regime increases. Note however that the drag coefficient for dimpled spheres in the post-critical regime is considerably higher than that of a smooth sphere. To investigate the origin of this behaviour Beratlis *et al.* (2019) carried out direct numerical simulations (DNS) of the flow over a dimpled sphere in the post-critical regime. By comparing the computed pressure and skin friction coefficients to that of a smooth sphere they showed that i) dimples decrease the overall skin friction drag, which rectifies the common assumption that dimples typically increase it; and ii) dimples, despite their small size, incur a local pressure penalty, which is significant and accounts for the most part of the difference in drag between a smooth and a dimpled sphere in the post-critical regime. The above study as well as earlier experiments in the literature point to the limitations of further reducing the total drag on a dimpled sphere without lowering the critical Reynolds number.

In this work we present a new topological configuration that can achieve a drag reduction of up to 15% compared to a dimpled sphere without shifting the drag crisis. The modification is based on the tessellation of the sphere resulting in spherical polyhedral containing mostly hexagonal and some pentagonal flat panels. An example of such a sphere is shown in Fig. 1. The drag on the tessellated spheres is measured by wind tunnel experiments that show that the low drag configuration is maintained through the post-critical regime. To under-

stand the flow physics a DNS of one spherical polyhedral and one dimpled sphere are carried out in the post-critical regime. Analysis showed that similar to dimples the sharp change in angle between the flat panels cause local flow separation leading to the formation of a detached shear layer that becomes unstable resulting in the generation of turbulence, which causes transport of high speed fluid closer to the wall.

METHODOLOGIES

Both wind tunnel experiments and direct numerical simulations have been carried out. The experiments have been carried out in an open return wind tunnel at the George Washington University with a test section of $30cm \times 25cm \times 70cm$ in the spanwise, vertical and streamwise direction respectively running at speeds between 18-63 m/s. The drag force was measured using a single component piezoelectric force sensor mounted on a sting on one end and attached to the back of the spheres on the other end as illustrated in Fig. 2. The sensor had a diameter of $0.6cm$ and width of $0.2cm$. The sting itself was attached to a rigid test stand located approximately $20cm$ behind the spheres. A very thin piano wire $0.05cm$ in diameter was wrapped around the sting and securely attached to the floor of the test section to reduce the vibrations on the spheres. The models were 3D printed on the Projet 3500 printer and had a diameter of $6.85cm$ resulting in a blockage ratio of less than 5%. For validation the drag coefficient of a smooth sphere in the sub-critical regime ($8.0 \times 10^4 < Re < 2.2 \times 10^5$) was measured, and was in agreement to prior experiments in the literature.

For the numerical simulations the Navier-Stokes equations for viscous incompressible flow are solved on a structured grid in cylindrical coordinates. In the following and unless otherwise stated, the letters r, ϕ, and z denote the radial, azimuthal and axial coordinates respectively, while θ denotes the polar angle, going from $\theta = 0°$ at the stagnation point at the front of the sphere to $\theta = 180°$ at wake side. The governing equations are advanced in time using a semi-implicit projection method, treating the explicit part with a 3rd order Runge-Kutta scheme, and the implicit part with a 2nd order Crank-Nicholson scheme. All spatial derivatives are discretized using second-order central-differences on a staggered grid. To overcome the severe time step limitation imposed by the nature of the cylindrical coordinate grid, the viscous and convective terms are treated implicitly in the azimuthal direction, near the centerline, and in the radial direction near the top of the sphere. The pressure Poisson equation, which enables the projection of the predicted velocity into a divergence-free field, is solved using a direct solver based on a divide-and-concur strategy. All geometrical configurations considered here are represented by a Lagrangian grid consisting of triangular elements. The requirement for the Eulerian grid to conform to the body is relaxed, and the non-slip boundary conditions are imposed using the immersed-boundary formulation proposed by Yang & Balaras (2006). The resulting formulation is 2nd-order accurate both in space and time. An extensive validation on practical flow problems over a wide range of Reynolds numbers can be found in Balaras et al. (2015); Posa et al. (2011, 2015); Posa & Balaras (2016); Rahromostaqim et al. (2016); Pal et al. (2017); Posa & Balaras (2018). The code is parallelized using a domain decomposition approach in the streamwise direction, where all communication between processors is handled utilizing Message Passing Interface (MPI) library calls.

The computational domain extends $10D$ upstream and

Table 1. Summary of the computations

Name	V/V_s	A_f/A_{f_s}	$C_D(DNS)$
Dimpled	0.989	0.990	0.188
Poly192	0.979	0.986	0.155
Poly162	0.973	0.982	0.178

$30D$ downstream of the sphere (the center of the sphere is located at $r/D = 0$, $z/D = 0$, where r and z are the radial and axial coordinates respectively). The computational grid consists of $1100 \times 3002 \times 3002$ points in the radial, azimuthal and axial directions respectively. The grid resolution is very similar to the one used in DNS of the flow over a dimpled sphere by Beratlis et al. (2019), which is sufficient to resolve the dominant flow structures near the wall as well as in the near wake. The Reynolds number was set to $Re = 1.5 \times 10^5$. Approximately 1 flow-through time was required for the solution to become independent of the initial conditions. After that statistics were accumulated over 2.5 flow-through times. In the following and for a generic flow variable the lower case, β, represents an instantaneous quantity, the upper case, B, represents the variable averaged over time only, β' represent the instantaneous fluctuations for the time-averaged quantity, and $\overline{B}$, represents the variable averaged over both time and azimuthal direction.

DISCUSSION

Fig.1 shows the variation of the drag coefficient with Reynolds number measured in the wind tunnel for one dimpled sphere and for two polyhedral spheres, one with 162 and 192 polygonal panels (referred to from now on as poly162 and poly192 respectively). Some basic geometrical properties are listed in Table 1. The dimpled sphere contains 312 spherical dimples, with an average diameter, $d = 0.095D$, and maximum depth $k = 0.003D$. The resulting dimple coverage, which is the ratio of the surface area occupied by the dimples to the total surface of a sphere, is approximately 70%. The geometry is representative of a commercial golf ball. The dimpled sphere has the largest volume of the three, about 0.989 of that of a sphere with $D = 1$, followed by poly192 and poly162. The ratio of frontal area to that of a smooth sphere is also very close to 1 for all spheres, with the dimpled sphere, poly192 and poly162 being 0.990, 0.986 and 0.982 respectively. Therefore the reduction in the drag coefficient exhibited by the above polyhedral and shown next can not be attributed to changes in the frontal area.

The drag curves for the polyhedral and dimpled spheres are very similar, with the polyhedral exhibiting a drag crisis around $Re \sim 8 \times 10^4$ and maintaining the low drag in the post-critical regime. In general, as the number of polygonal panels increases, the polyhedral approaches a smooth sphere and the drag crisis shifts towards higher Reynolds numbers while the drag coefficient in the post-critical regime decreases. It is important to note that the drag crisis for poly192 appears to be occurring at the same critical Reynolds number as the dimpled sphere but the drag coefficient is consistently lower by $10\% - 15\%$ throughout the post-critical regime. For the poly162 the drag coefficient in the post-critical regime is almost identical to that of the dimpled sphere but the drag crisis occurs earlier. The predicted drag coefficient from the present DNS for poly192 and the dimpled sphere are also shown in the
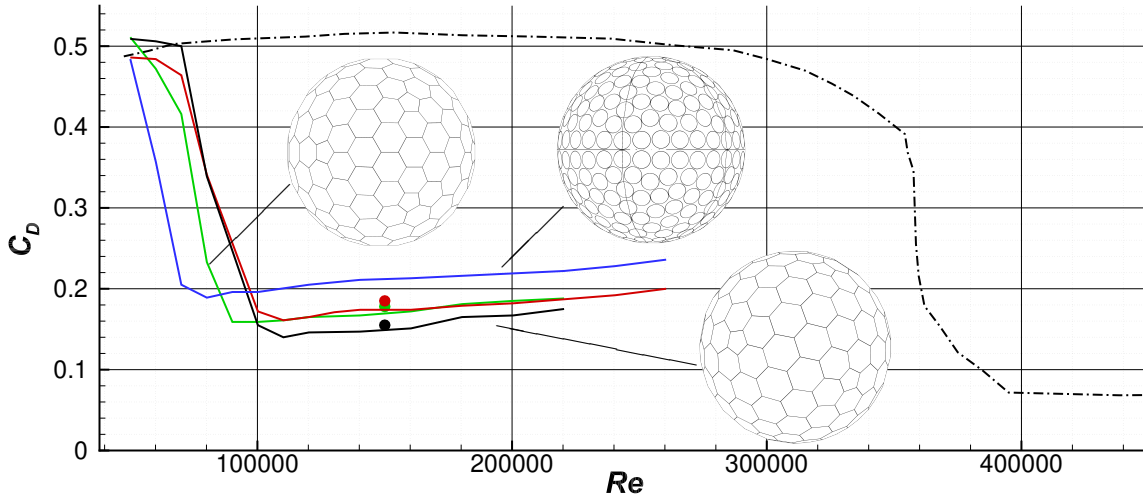
Figure 1.   Drag coefficient vs Reynolds number for various spheres. — · — smooth sphere Achenbach (1972); ——— dimpled sphere with dimple depth $k = 0.0035D$ (present experiment); ——— dimpled sphere with $k = 0.003D$ (present experiment); ——— icosahedral sphere with 192 polygonal panels (present experiment); ——— icosahedral with 162 polygonal panels (present experiment); ● icosahedral with 192 polygonal panels (present DNS); ● icosahedral with 162 polygonal panels (present DNS); ● dimpled sphere with $k = 0.003D$ (present DNS).
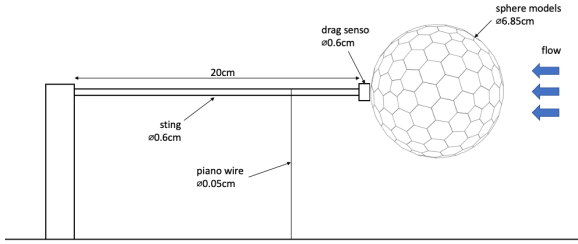
Figure 2.   Wind tunnel setup for measuring the drag force

plot. The agreement with the experimental results is very good with the DNS values are within 2-3% of the experiments. The drag coefficient for the dimpled sphere is 0.185, while that for poly192 is 0155 (16% lower).

It is clear from the behaviour of the force coefficients that the polyhedral designs are more efficient in reducing the drag than the dimples. To better understand this behavior we will compare the results from the corresponding DNS. Fig. 3 shows contours of the time-averaged skin friction coefficient, $\overline{C_f}$, for the dimpled sphere and poly192. The skin friction was calculated as, $C_f = 2v/U^2 \cdot dU_t/dn$, where U_t is the tangential velocity minus the azimuthal component and n is the surface normal. The separation line is indicated by a black line and the polar angle θ measured from the stagnation point at the front is denoted by vertical dashed lines. For the dimpled sphere the flow separates locally inside some dimples as early as $50°$ and remains attached at the next row of dimples. Small local separation bubbles are again observed at $70°$ and they appear to be present more consistently in the azimuthal direction. Larger local separation bubbles occupying the first half of the dimples occur at the next row of dimples around $\theta = 80°$. For poly192 the behavior of the skin friction is very different. A couple of small separation bubbles appear around $\theta = 80°$ and more consistently in the azimuthal direction around $\theta = 90°$

Fig. 4a shows the skin friction coefficient, $\overline{C_f}$, averaged over time and the azimuthal direction. The average surface depth distribution k/D is also plotted at the bottom. The depth is measured relative to the surface of a smooth sphere of di-

ameter D. For the case of the dimpled sphere k/D exhibits considerable variation while for poly192 it is more uniform and also consistently higher. For the former, $\overline{C_f}$ exhibits local peaks and valleys consistent with the presence of the dimples, while for poly192 it is considerably smoother. Global separation, identified as the cross from positive to negative values of C_f, occurs at $\theta = 116°$ and $\theta = 126°$ for the dimpled and polyhedral spheres respectively. The integral of the skin friction as a function of θ is shown in Fig. 4b. When the integral is evaluated over the entire sphere it is equal to the skin friction drag. In the front part of both spheres ($\theta < 45°$) the integral of the skin friction is very similar. For $\theta > 45°$ the skin friction drag for the tessellated sphere is slightly larger than that of the dimpled sphere. This is expected since for poly192 the flow remains attached for longer than the dimple sphere. Overall the skin friction drag for both spheres is less than 10% of the total drag.

The distribution of the average pressure coefficient, $\overline{C_p}$, together with the average surface depth, k/D, as a function of θ is shown in Fig. 5a. For poly192, $\overline{C_p}$ is relatively smooth while for the dimpled sphere it exhibits small oscillations that are correlated with the average dimple depth. In particular, the local peaks in $\overline{C_p}$ occur slight after local maxima in k/D and vice versa. At the back of the sphere ($90° < \theta < 125°$) $\overline{C_p}$ for poly192 is lower. However due to the delayed separation it recovers to a greater value and remains consistently higher than that of the dimpled sphere. As for $\overline{C_f}$ above, the integral of C_p as a function of θ is shown in Fig. 5b. For $0° < \theta < 45°$ the pressure integrals are very close. For $\theta > 45°$ the dimples start to incur a small pressure penalty relative to the polygonal panels. By $\theta = 90°$ the dimples contribute approximately 30% of the total drag *penalty*. At the back the remaining 70% contribution to the additional drag for the dimpled spheres comes form the lower back pressure due to the earlier separation.

The difference in the separation point between the two types of spheres can be explained by looking at the evolution of the boundary layer. First of all, the approximate location of transition to turbulence can be determined by looking at the behavior of the velocity fluctuations. Fig. 6 shows the variation of the turbulent kinetic energy, $\overline{q}$, averaged over time and in the

azimuthal direction. The quantity is plotted along an arc that has a radius of $0.505D$, that is $0.005D$ above the surface of a smooth sphere. The points on that arc are shown with markers in the subset. The levels of q are negligible at the front part for both spheres and they start to rise around $\theta = 75°$ and $\theta = 87°$ for the dimpled sphere and poly192 respectively. It is therefore reasonable to assume that transition to turbulence is delayed for the latter case. The location of the peak in q also occurs a little later but overall the maximum levels of q are similar.

Fig. 7 shows contours of the instantaneous azimuthal vorticity at a plane cutting through the middle of a dimple near the top of poly192 sphere where transition occurs. Contours of the instantaneous skin friction coefficient, C_f, are plotted on the surface of the sphere along with the separation line denoted by a black line. It is clearly seen that a shear layer is formed as the flow separates over the leading edge of the flat hexagonal panel. The flow separation is not uniform across the span and occurs over a small portion near the first half of the panel. The flow reattaches again near the center of the panel. Shortly after the flow separates the shear layer becomes un-
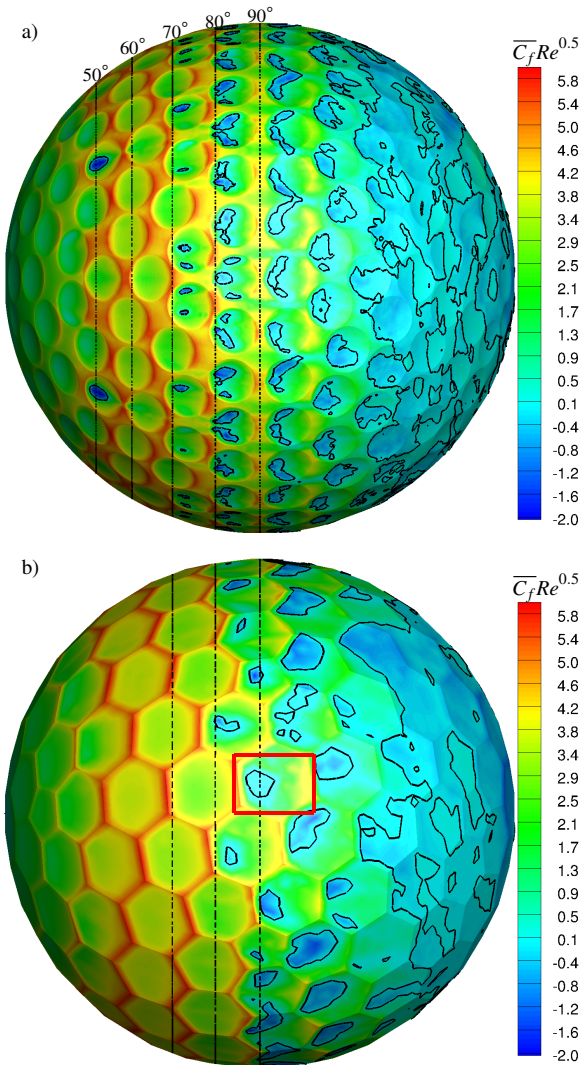

Figure 4. a) Distribution of the average skin friction coefficient, C_f, (top part) and average surface depth (bottom part); b) Integral of C_f. ——— dimpled sphere; ——— poly192; ——— difference between dimpled sphere and poly192.

a)

b)

Figure 3. Contours of the time-average skin friction coefficient, $\overline{C_f}$, scaled by $Re^{0.5}$. a) dimpled sphere; b) poly192. The separation line is shown with a solid black line while the polar angle at various locations is indicated by vertical dashed lines. The red rectangular outline corresponds to the location of the hexagonal dimple shown in Fig. 7.
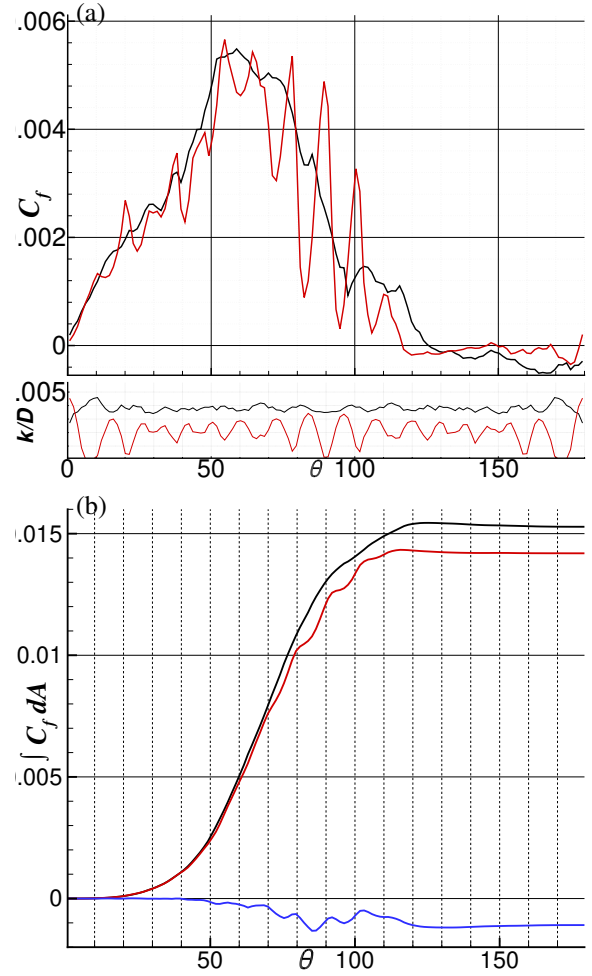
stable and starts to roll-up into vortical structures, annotated as rollers A and B in the figure. The evolution of these rollers, which is essential in the transition process, can be better traced in Fig. 7b, where a top view is shown and the vortical structures are colored by their streamwise vorticity. It can be seen that roller A is not uniform in the azimuthal direction and does not extend across the entire span of panel. A similar behaviour can be observed for roller B. As these rollers undergo instabilities in the azimuthal direction their vorticity is reoriented from the azimuthal to the streamwise direction. Also, in between the two rollers pairs of counter-rotating streamwise vortices are present. These vortices are reminiscent of the braid-vortices containing mainly streamwise vorticity of opposite sign, typically found in free-shear layers undergoing Kevin-Helmhotz type instability. Towards the end sides of the rollers thin elongated vortices aligned in the sreamwise direction and containing streamwise vorticity are observed. Farther downstream and close to the trailing edge of the dimple various vortical structures resembling a Λ-type vortex are clearly observed. This pack of Λ-type vortices has evolved from the continuous bending of a previously shed roller and its legs are connected to a pair of braid vortices. We should note that the rollers aligned primarily in the azimuthal direction are transformed into Λ-type vortices always within the length of one panel for a given Reynolds number. This mechanism is qualitatively similar to the one observed for flow over a dimpled

4

sphere Beratlis *et al.* (2019).

To further quantify this, profiles of the time averaged streamwise velocity and turbulent kinetic energy around $\theta = 83°$ are shown in Fig. 8. Three stations are selected: one before, one inside and one after the shear layer where transition takes place. At the first station the velocity profile and the lack of turbulent kinetic energy confirms that the boundary layer is still laminar. In the second station the negative velocity near the wall indicates the flow and the velocity profile resembles that of a shear layer. The turbulent kinetic energy has a sharp peak at approximately $r/D = 0.0035$ indicating that the shear layer become unstable. Farther downstream near the trailing edge of the hexagonal panel the peak in the turbulent kinetic energy moves closer to the wall, at $r/D = 0.017$. However the profile of q is much broader with significant levels of turbulent kinetic energy extending up to $r/D = 0.012$. This is characteristic of momentum transport across the boundary layer.

Fig. 9 shows the average boundary layer thickness, δ, as a function of the polar angle θ, up to the separation point. Since the location of the wall varies in the azimuthal direction the boundary layer thickness is first calculated at each azimuthal plane, as shown in the insert of Fig. 9. This gives a set of displacement thicknesses δ_1, δ_2, ..., $\delta_{n\phi}$ with respect to the local wall location, which are then averaged over the azimuthal direction ϕ to give $\overline{\delta}$. Note that $\overline{\delta}$ is calculated utilizing the vor-

Figure 6. Variation of the turbulent kinetic energy, $\overline{q}$, along an arc line with radius $R = 0.505D$. ——— poly192; ——— dimpled sphere. The inset on the top left shows contours of $\overline{q}$ for poly192 with black dots representing the arc line.
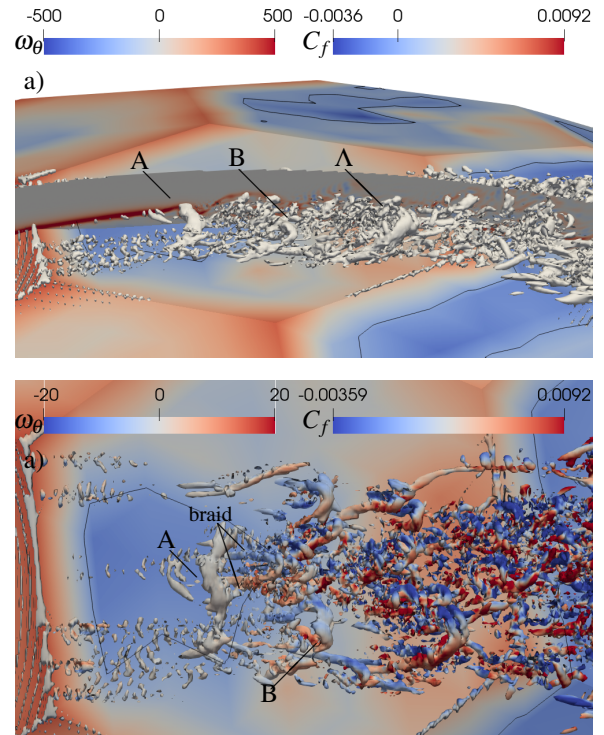
Figure 7. a) Isosurface of the *Q-criterion* visualizing vortical structures near the top of the tesselated sphere. Contours of the instantaneous azimuthal vorticity, ω_θ, are also shown at an azimuthal plane going through the middle of a hexagonal panel along with contours of the instantaneous skin friction, C_f, plotted on the surface of poly192. The separation line is denoted by solid black line. The location of the hexagonal panel is indicated with a red box in Fig. 3b. b) Top view with vortical structures colored by contours of tangential vorticity ω_t.
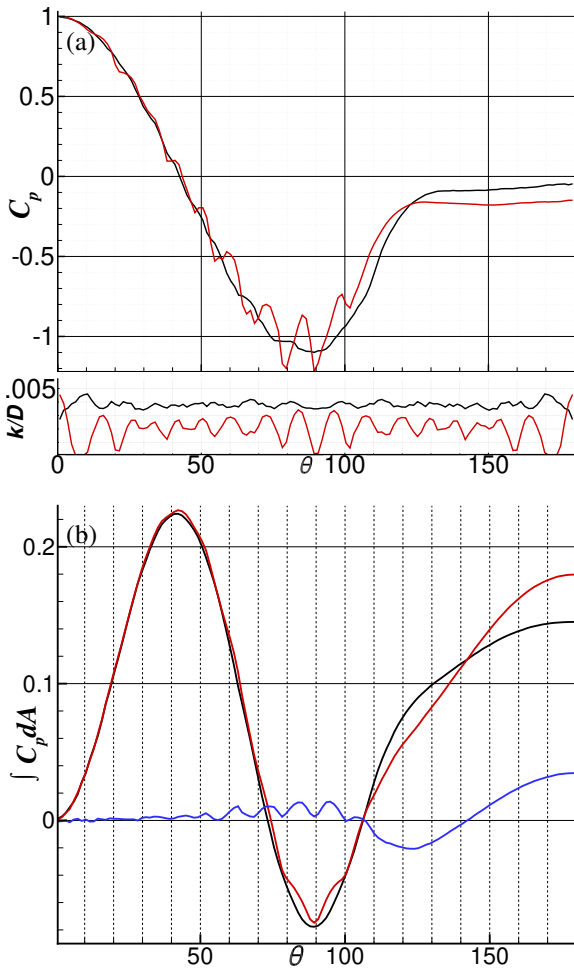

Figure 5. a) Distribution of the average pressure coefficient C_p (top part) and average surface depth (bottom part); b) Integral of C_p. ——— dimpled sphere; ——— poly192; ——— difference between dimpled sphere and poly192.
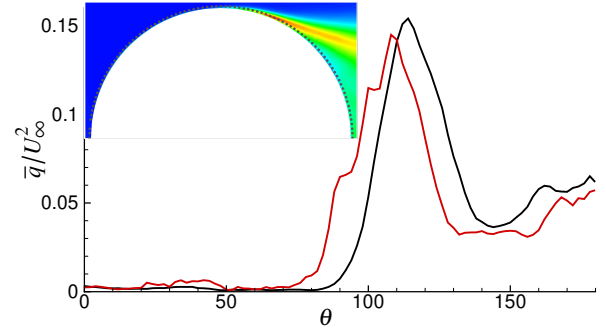
ticity definition proposed by Spalart & Watmuff (1993), which is more appropriate in the presence of curvature and pressure gradients. For the dimpled sphere the boundary layer does not grow in a monotonic fashion, and there are local peaks and valleys associated with the presence of the dimples (for reference the average dimple depth is shown on the lower part of the figure). The peaks and valleys in $\overline{\delta}$ correspond to the location of the maximum and minimum dimple depth respectively, and overall dimples promote a thickening of the boundary layer.
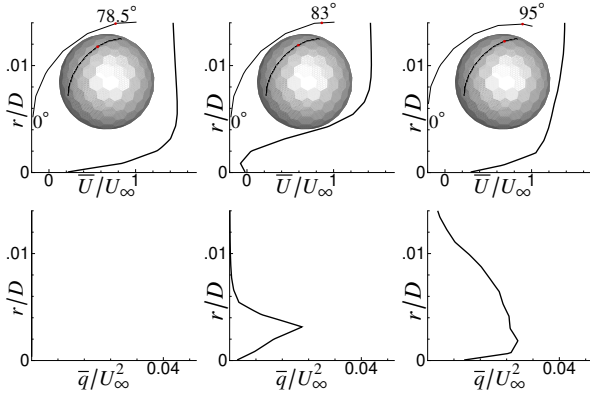
Figure 8. Top part: Profiles of the time averaged streamwise velocity U; Bottom part: profiles of the mean turbulent kinetic energy q. Statistics are shown at three stations along an azimuthal plane. The locations of the stations are also indicated in the figure: A is at $\theta = 78.5°$, B is at $\theta = 83°$, C is at $\theta = 95°$
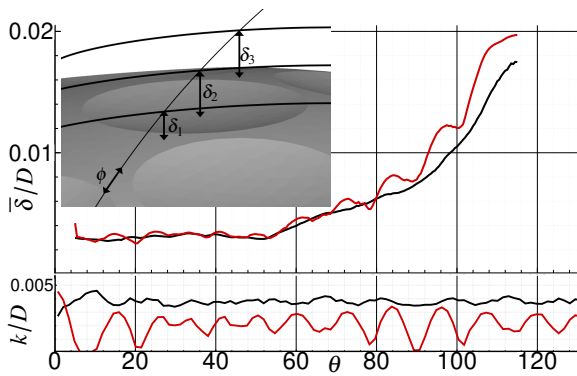

Figure 9. Plot of the boundary layer thickness $\overline{\delta}$ averaged over time and azimuthal direction and average dimple depth k/D. Lines represent: –; poly192, –; dimpled sphere

For poly192 the boundary layer growth is smoother.

SUMMARY

Dimples have been long considered as an efficient mechanism for tripping the boundary layer and reducing drag on spheres. Previous work by the authors revealed though that dimples impose a significant pressure penalty which can hinder drag reduction. The authors present a novel topological modification, comprising the tessellation of a sphere, that can reduce drag even more without changing the Reynolds number at which the drag crisis occurs.

We report wind tunnel measurements of the drag coefficient over a range of Reynolds numbers, as well as DNS for selected cases in the post-critical regime. Dimpled and tessellated spheres are considered. The wind tunnel measurements demonstrate that the variation of the drag coefficient as a function of the Reynolds number for the two tessellated sphere cases is very similar to that of dimpled spheres: drag crisis occurs and the drag coefficient remains relatively constant in the post-critical regime. As the number of tessellations increases the drag crisis shifts towards higher Reynolds number and the value of the drag coefficient in the post-critical regime is reduced.

Detailed analysis of the results from the numerical simulations showed that a tessellated sphere reduces the pressure *penalty* compared to dimples while also delaying separation

by 10° at the same Reynolds number. Transition to turbulence on a dimpled sphere also occurs closer to the stagnation point. As a result the boundary layer grows thicker and the flow separates earlier giving rise to lower back pressure and higher form-drag.

REFERENCES

Achenbach, E. 1972 Experiments on the flow past spheres at very high reynolds numbers. *Journal of Fluid Mechanics* **54** (3), 565–575.

Balaras, E., Schroeder, S. & Posa, A. 2015 Large-eddy simulations of submarine propellers. *Journal of Ship Research* **59** (4), 227–237.

Beratlis, Nikolaos, Balaras, Elias & Squires, Kyle 2019 On the origin of the drag force on dimpled spheres. *Journal of Fluid Mechanics* **879**, 147–167.

Pal, A., Sarkar, S., Posa, A. & Balaras, E. 2017 Direct numerical simulation of stratified flow past a sphere at a subcritical reynolds number of 3700 and moderate froude number. *Journal of Fluid Mechanics* **826**, 5–31.

Posa, A. & Balaras, E. 2016 A numerical investigation of the wake of an axisymmetric body with appendages. *Journal of Fluid Mechanics* **792**, 470–498.

Posa, A. & Balaras, E. 2018 Large-Eddy Simulations of a notional submarine in towed and self-propelled configurations. *Computers and Fluids* **165**, 116–126.

Posa, A., Lippolis, A. & Balaras, E. 2015 Large-eddy simulation of a mixed-flow pump at off-design conditions. *ASME Journal of Fluids Engineering* **137** (10), 101302.

Posa, A., Lippolis, A., Verzicco, R. & Balaras, E. 2011 Large-eddy simulations in mixed-flow pumps using an immersed-boundary method. *Computers & Fluids* **47** (1), 33–43.

Rahromostaqim, M., Posa, A. & Balaras, E. 2016 Numerical investigation of the performance of pitching airfoils at high amplitudes. *AIAA Journal* **54** (8), 2221–2232.

Spalart, P. R. & Watmuff, J. H. 1993 Experimental and numerical study of a turbulent boundary layer with pressure gradients. *Journal of Fluid Mechanics* **249**, 337–371.

Yang, J. & Balaras, E. 2006 An embedded-boundary formulation for large-eddy simulation of turbulent flows interacting with moving boundaries. *Journal of Computational Physics* **215** (1), 12–40.